Acta Geotechnica
https://doi.org/10.1007/s11440-020-00975-z

RESEARCH PAPER

Measurement of local and volumetric deformation in geotechnical triaxial testing using 3D-digital image correlation and a subpixel edge detection algorithm

Pengpeng Wang[1,2] · Xiaoxia Guo[2] · Yong Sang[3,4] · Longtan Shao[2] · Zenan Yin[2] · Yudi Wang[2]

Received: 19 April 2019 / Accepted: 14 April 2020
© Springer-Verlag GmbH Germany, part of Springer Nature 2020

Abstract
Based on the three-dimensional digital image correlation (3D-DIC) technique, the stereovision system has been applied to the improved triaxial apparatus to obtain 3D full-field deformation of the specimen during triaxial testing. Through the calibration process, the 3D-DIC technique can obtain the accurate specimen's spatial displacement deformation. Meanwhile, a subpixel edge detection algorithm has been combined with 3D-DIC technique to calculate the radial strain and the volume strain of the specimen directly. Furthermore, a series of consolidated drained and undrained triaxial tests were carried out on Hainan (China) sand specimens and measured by the conventional and the image measurement methods. Compared to the results measured by the conventional method, the image measurement technique can obtain the more experimental data, such as the 3D displacement field of the whole specimen, the local strain distribution, and so on. The measurement results also show the conventional method would be disturbed by the end constraints in triaxial tests so that the strength of the soil would be overestimated. Meanwhile, the middle of the specimen would be selected to calculate the stress–strain relationship without the influence of the end constraints in the proposed method. Based on the image measurement results, the proposed method has the potential to be used in geotechnical tests for exploring the soil's progressive failure behaviors, inhomogeneous deformation and mechanical characteristics.

Keywords 3D-DIC · Inhomogeneous deformation · Progressive failure · Subpixel edge detection algorithm · Triaxial test

1 Introduction

Local deformation and total deformation of a soil specimen play important roles in understanding the characteristics of anisotropy and nonlinearity in geotechnical materials. At the same time, these parameters are also essential in theoretical modeling and numerical simulations of soil mechanics, for example, for volumetric strain, soil stiffness and shear band characterization. Only the total volume change of a saturated soil specimen and the total vertical change of saturated and unsaturated soil specimens can be obtained using a conventional triaxial apparatus. Because saturated soil is only composed of water and soil solids, total volume changes can be measured according to the pore water volume exchange of the specimen, but local deformation cannot be measured with a conventional triaxial apparatus. Unsaturated soil includes air in addition to water and soil solid, so that the conventional method

✉ Xiaoxia Guo
hanyuer@dlut.edu.cn

[1] Mechanical and Electrical Engineering Institute, Zhengzhou University of Light Industry, No. 5, Dong Feng Road, Zhengzhou City 450002, Henan Province, China

[2] Department of Engineering Mechanics, Dalian University of Technology, No. 2, Ling Gong Road, Dalian City 116024, Liaoning Province, China

[3] Key Laboratory for Precision and Non-Traditional Machining Technology, Ministry of Education, Dalian University of Technology, Dalian City 116024, Liaoning Province, China

[4] School of Mechanical Engineering, Dalian University of Technology, Dalian City 116024, Liaoning Province, China

Published online: 25 May 2020

cannot be fully accurate for measuring local and total volume changes to characterize the soil specimen through the measurement of the pore water volume change. As a result, the conventional triaxial apparatus has limitations for the measurement of the local and total deformation of soil specimens. Over the past few decades, many research efforts have been made to develop to measure total or local deformation in triaxial experiments.

The current methods for measuring the deformation of soil specimens can be broadly classified into three categories: (1) direct measurement of axial and radial dimensions by local displacement sensors, (2) calculation of the specimen's total volume changes from the measurement of fluid exchange, and (3) direct measurement of the specimen's local or full-field deformation using various optical and computer vision technologies.

For the methods in the first category, researchers generally use several miniature linear variable differential transformers (LVDTs) for the direct measurement of axial and radial displacements to directly assess the volumetric strain in triaxial soil tests [2, 18, 30]. The accuracy of these LVDTs is as high as 3 μm, and LVDTs can capture a wide range of strains between 10^{-6} and 10^{-2} to measure the local small strain [31]. However, this method also has obvious disadvantages. The sensors must contact the specimen in the experiment and may affect the deformation of the specimen, particularly for soft soil. Meanwhile, very complicated and time-consuming procedures must be used for the installation of the sensors for every test. Generally, local displacements are measured by only one to three LVDTs, so the measurement of volume changes may become significantly inaccurate, such as in the case of an inhomogeneous deformation of the specimen [13], and the methods in this category cannot obtain full-field deformations of the specimen.

The methods in the second category provide a straightforward approach for measuring the total volume changes of a specimen and are suitable for application to unsaturated soil specimens. This category can be further divided into the direct measurement of air and water volume changes separately, in the specimen: measurement of the chamber's fluid discharge [3, 19]; and measurement of the specimen's total volume changes using double-wall systems [5, 28]. The methods in the second category can accurately obtain total volumetric changes. The accuracy of the results for a triaxial specimen in total volumetric strain measurements can reach 0.04% [19]. However, the methods in this category cannot obtain local deformation. At the same time, experiments performed with the methods in this category have high apparatus requirements and require careful calibration. The results of these experiments are sensitive to temperature, liquid leakage and atmospheric pressure, and de-aired water is required.

The third category is the non-contact method. Examples of this approach include the use of laser scanners [16, 35, 37], X-ray computed tomography [10, 12], digital image analysis based on feature matching [14, 17, 22, 33, 36], and digital image correlation (DIC) [21, 29]. Messerklinger et al. [16] measured the radial displacement of a specimen over the height of the entire specimen in triaxial testing apparatuses using three laser scanners and determined the volume change during the experiment. The resolution of the device was ± 1 μm, and the accuracy of the radial strain measurement results reached 0.04%. X-ray computed tomography (CT) can directly observe the true kinematics of particles in a specimen and can be used to analyze the void ratio evolution, shearing and grain breakage. More recently, high-resolution X-ray CT (μCT) combining several tracking methods has been proposed for quantitative analysis of the particle distribution of a specimen [1, 6, 11]. X-ray CT reached a spatial resolution of 5 μm [11]. However, the laser scanner and X-ray CT are unsuitable for widespread use because these devices require sophisticated and costly installation procedures, and the use of X-ray CT may pose risks to health. These devices are also not suitable for dynamic loading experiments due to their inefficient operation. With the development of computer vision and the increasing availability of digital cameras, digital image measuring (DIM) techniques are becoming more attractive. Digital image analysis based on feature matching is a convenient method in practical applications; for example, Shao et al. [23] recognized the grid points on the surface of a membrane (with a soil specimen inside) based on feature matching to obtain the two-dimensional (2D) full-field deformation of a specimen's entire circumferential surface. Zhang et al. [36] and Li and Zhang [14] determined the three-dimensional (3D) deformation of a soil specimen through a photogrammetric approach. However, if an insufficient number of markers based on feature matching are used, the obtained anisotropic deformation results will be inaccurate. Generally, only several hundreds of marker points on the surface of the membrane are used in these methods. This number of points is not sufficient to represent the deformation. The DIC technique is also an image-based deformation measurement technique based on digital image processing and numerical computation. The gray value of every pixel in the reference image is utilized to track their respective locations in the deformed images in this method. Therefore, it is common to track tens of thousands calculation points in every image. Since it has been improved by Sutton [24], this method is becoming very popular in measuring the full-field deformation of materials. In recent years, some researchers have proposed several advanced algorithms to improve the calculation speed, robustness and accuracy of DIC [9, 20, 32]. The 3D-

DIC technique is based on the 3D reconstruction of the stereovision system and the tracking algorithm of the 2D-DIC [4, 25]. Tang et al. [26] explored the effects of the confining pressure on the progressive failure behaviors of rocks using 3D-DIC with six cameras. The full-field strains and crack evolution of the specimen were obtained by the 3D-DIC method. Generally, the digital image technique can reach subpixel accuracy. Although the DIC method (2D-DIC and 3D-DIC) has been used for many solid mechanics studies, it has found only limited application in studies of soil mechanics because soil mechanics experiments are different from convenient solid mechanics testing. The soil specimen must be placed in a hermetic chamber and tested under confining pressures. These experiments also require the use of more complex procedures.

In this work, an improved triaxial apparatus was developed in our laboratory based on the 3D-DIC technique to precisely obtain local and global deformation from the surface of soil specimens and photogram metrically reconstruct a digital 3-D model. At the same time, a series of consolidated drained and consolidated undrained triaxial tests were carried out on Hainan (China) sand samples using this apparatus. Combining the subpixel edge detection algorithm with the 3D-DIC technique, not only the progressive failure behaviors of sands in different confining pressures were explored but additional deformation properties such as the radial strain distribution and local volume changes of the cylindrical soil specimen were also obtained in triaxial testing. Finally, according to the results measured by the proposed method, the soil's local deformation and mechanical characteristic have been discussed.

2 Experimental methodology

2.1 Experimental apparatus and digital image measurement system

Experiments were conducted in an electro-hydraulic servo static-dynamic triaxial apparatus designed by the State Key Laboratory of Structural Analysis for Industrial Equipment in Dalian University of Technology. The principle of control is based on the electro-hydraulic servo technique, which applies an adaptive fuzzy sliding mode control method to improve the tracking error, as shown in Fig. 1a. To capture the specimen image, the pressure chamber was redesigned to bear a pressure of 1 MPa, and a pane of tempered glass was installed in the front of the pressure chamber. Additionally, two sets of LED lights were installed in the pressure chamber to provide a stable light source to avoid light reflection of external light source, as shown in Fig. 1b. Confining pressure was applied to the specimen using compressed air with a small refractive index that could not give rise to specimen image distortion. The image acquisition system composed of two CCD cameras was placed in front of the pressure chamber to capture the specimen image. A schematic diagram of the stereovision measurement system is shown in Fig. 1c. Two cameras with different view angles capture two-dimensional images in the same area of the object, and 3D structure reconstruction was realized according to the triangulation principle and bundle adjustment. During triaxial tests, two digital images were simultaneously recorded every 5 s using two 14-bit Pike F-100B/C (1000 × 1000 pixels) digital cameras which were made by Allied Vision Technologies (AVT) in Germany.

2.2 Experimental procedure and specimen preparation

The sand used for the experiments was taken from Hainan (China) province. The sand particle size distribution is shown in Fig. 2, and the properties of this sand are listed in Table 1. All specimens were constructed using a standard cylindrical mold following vibratory compaction methods and had a diameter and height of 61.8 mm and 125 mm, respectively. Fully saturated specimens were prepared by displacing the air in the specimen by CO_2 for 2 h and then passing de-aired water through the sample. Four sets of consolidated drained triaxial compression tests and three sets of consolidated undrained triaxial compression tests were carried out on these specimens at three different confining pressure: 100 kPa, 200 kPa, and 300 kPa, and the test was repeated three times under the same confining pressure. The back pressure saturation method also was applied to the triaxial tests, and the saturation values of all specimens are greater than 98.5%. All of the specimens were sheared at a constant strain rate of 0.2%/min after consolidation. The displacement of the actuator was measured using a linear variable differential transformer (LVDT). The initial experimental characteristics, such as the test name, confining pressure, test condition, initial density of specimen and initial relative density, are listed in Table 2. According to the initial relative density, the specimens of HnCD-111, HnCD-121, HnCD-131, HnCU-111, HnCU-121 and HnCU-131 are in a dense state; the specimen of HnCD-211 is a medium dense state; "HnCD" represents consolidated drained triaxial compression test and "HnCU" represents consolidated undrained triaxial compression test for Hainan sand. Meanwhile, an irregular grayscale value on the specimen surface is required in the DIC method, such as the speckle pattern and natural pattern of materials. In this study, because the specimen was wrapped by a membrane, the irregular pattern was created by spraying black and white paints on the membrane until

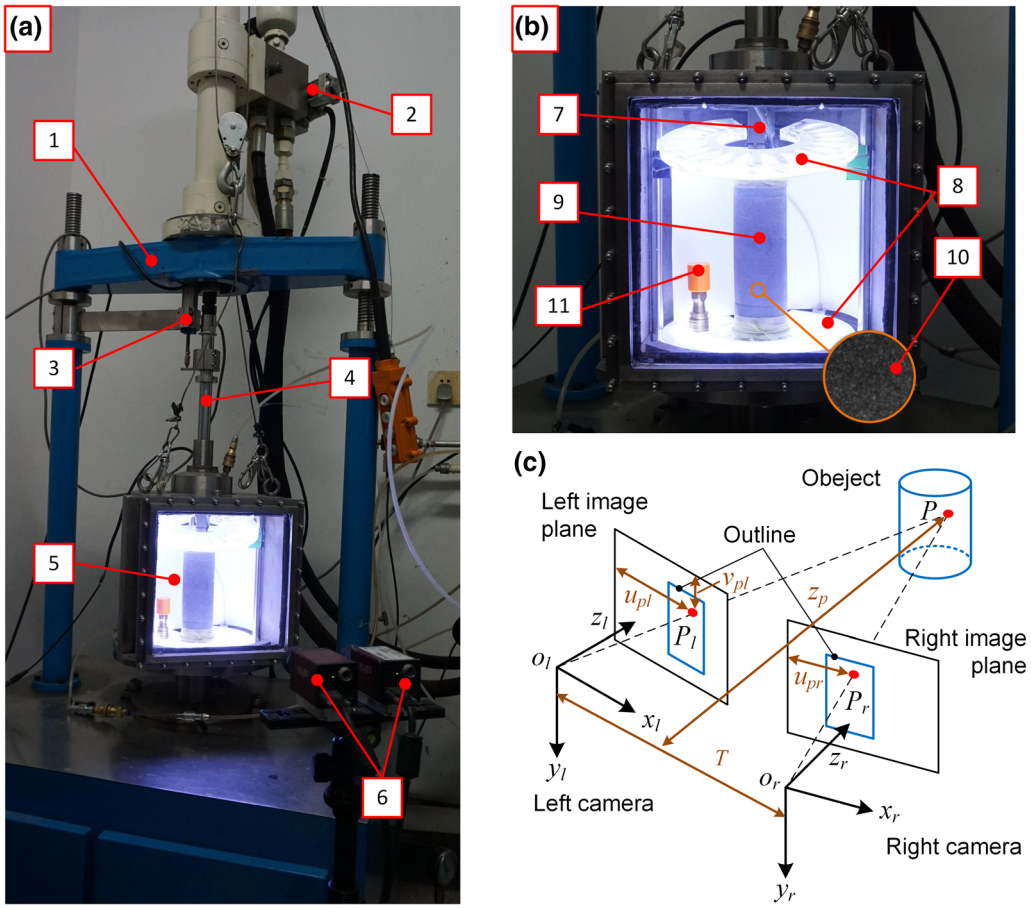

Fig. 1 **a** Experimental apparatus. **b** Components of the pressure chamber. **c** Principle of 3D rectification. 1—Experimental apparatus; 2—hydraulic servo valve; 3—linear variable differential transformer (LVDT); 4—loading rob; 5—pressure chamber; 6—stereovision system; 7—loading cell; 8—LED lights; 9—soil specimen; 10—speckle; 11—static reference object (color figure online)

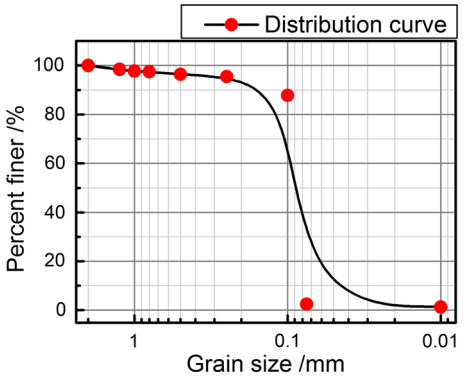

Fig. 2 Grain size distribution curve for Hainan sand (color figure online)

the irregular random distribution with a high contrast was obtained, as shown in Fig. 1b.

2.3 Realization of 3D-DIC

The principle of stereovision is shown in Fig. 1c. The pinhole camera model is proposed. A 3D point (P) on the object is recorded by the cameras (left camera and right camera) and corresponds to the two projective points (P_l and P_r) in the left and right image planes. After the stereovision system was calibrated, the 3D position of point (P) was obtained based on the similar triangles theorem. The spatial position of the point (P) in the camera coordinate system can be obtained using Eq. (1).

Table 1 Properties of experimental sands

Sand name	Average grain diameter D_{50} (mm)	Maximum void ratio e_{max}	Minimum void ratio e_{min}	Specific gravity G_s	Uniformity coefficient C_u	Curvature coefficient C_c
Hainan sand	0.089	0.972	0.597	2.679	2.14	1.23

Table 2 Experimental parameters of triaxial tests

Test name	Confining pressure σ_3 (kPa)	Test condition[a]	Initial density ρ_d (g/cm^3)	Initial relative density D_r (%)	Initial height H (mm)	Initial average diameter D (mm)	Physical length per pixel (mm/pixel)
HnCD-111	100	CD	1.597	78.4	124.26	61.68	0.1945
HnCD-121	200	CD	1.602	80.0	124.52	61.94	0.1962
HnCD-131	300	CD	1.626	86.4	124.08	61.36	0.1965
HnCD-211	100	CD	1.515	54.4	124.65	61.50	0.1911
HnCU-111	100	CU	1.617	84.0	123.28	61.77	0.1935
HnCU-121	200	CU	1.602	79.7	124.32	61.83	0.1947
HnCU-131	300	CU	1.605	80.8	124.06	61.98	0.1969

[a]CD represents consolidated drained triaxial compression test; CU represents consolidated undrained triaxial compression test

$$\begin{cases} x_p = \dfrac{u_{pl} \cdot T_x}{u_{pl} - u_{pr}} \\ y_p = \dfrac{v_{pl} \cdot T_x}{u_{pl} - u_{pl}} \cdot \dfrac{d_V}{d_H} \\ z_p = \dfrac{f \cdot T_x}{(u_{pl} - u_{pr}) \cdot d_H} \end{cases} \quad (1)$$

Here, x_p, y_p, z_p are the spatial coordinates from the point (P) in the left camera coordinate system, mm, and u_{pl} and u_{pr} are the horizontal pixel coordinates that the point (P) in the left and the right image views at P_l and P_r, pixel, respectively. d_H is the physical length of one pixel in the horizontal direction, mm. d_V is the physical length of one pixel in the vertical direction, mm. v_{pl} is vertical pixel coordinates that the point (P) in the left image views at P_l, pixel. f is the focus of the camera, mm. T_x is the horizontal distance from the right camera to the left camera, mm, and it is the horizontal component of T in Fig. 1c.

To improve accuracy, it is necessary to calibrate the stereovision system using methods such as undistortion and stereo correspondence and to obtain the physical dimension represented by a single pixel. Figure 3a, b presents two types of calibration targets. The chessboard plane in Fig. 3a can rectify the distortion of the cameras and realize stereo correspondence by obtaining the relative position between the two cameras in the stereovision based on bundle adjustment [34]. In order to avoid the specimen's images change caused by the uncertain factors during the test, a static reference object is placed into the pressure chamber with the specimen during the test, as shown in Fig. 1b (No. 11). If the size of the static reference object changes in the captured images, it would indicate that there is image distortion during the test. The specimen's images would be rectified according to the size change scale of the static reference object. In Fig. 3b, this is a stereo calibration object which can determine the relative position between the stereovision system and the triaxial apparatus. Some black squares with a side length of 5 mm are printed on the stereo calibration object and are separated from each other by 5 mm. When it is placed on the specimen base of the triaxial apparatus, the corners of these squares can be recognized by the corner recognition algorithm based on the subpixel Harris corners detection using the stereovision system [8]. Based on the principle of stereovision, the surface of the stereo calibration object can be reconstructed in camera coordinate system and the spatial pose of the surface relative to stereovision system can be obtained. Thus, the incline of the specimen relative to stereovision system can be rectified according to the spatial pose of the stereo calibration object. At the same time, according to these fixed-size black squares, the average physical length can be obtained given how many millimeters a pixel represents, as listed in Table 2. The procedure for performing the 3D-DIC measurement was independently developed by our laboratory in this work, as shown in Fig. 3c. The first image from the left camera is considered to be the reference image, and other images are deformed images. This strategy can reduce cumulative errors. The points or subsets of the object are tracked through the correlation function. In every pair of images, the same points or subsets in the left and right cameras can also be found through the correlation function. Then, for every point on the object, their corresponding projective points in the left and right cameras can be obtained. The positions of the 3D points are calculated using the 3D reconstruction program.

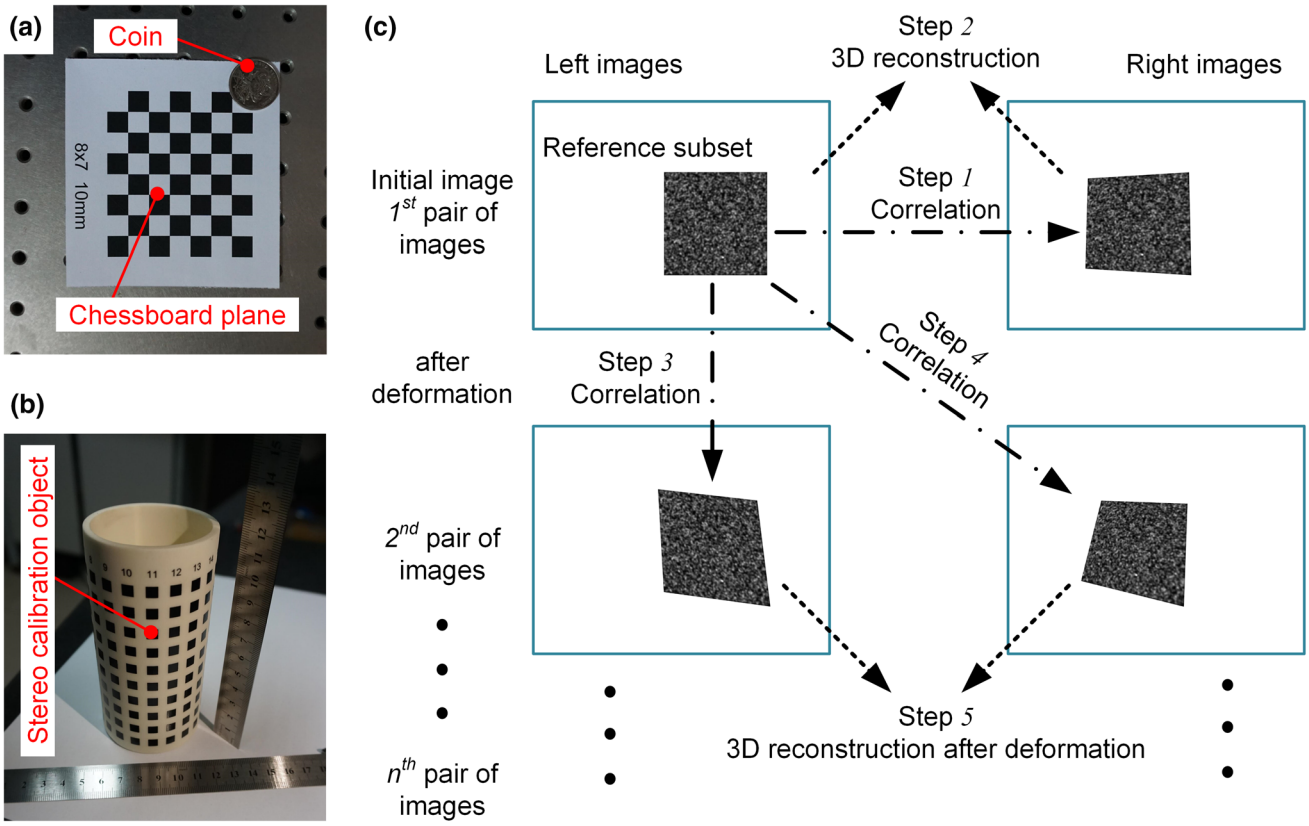

Fig. 3 **a** Chessboard plane. **b** Stereo calibration object. **c** Procedure for realizing 3D-DIC (color figure online)

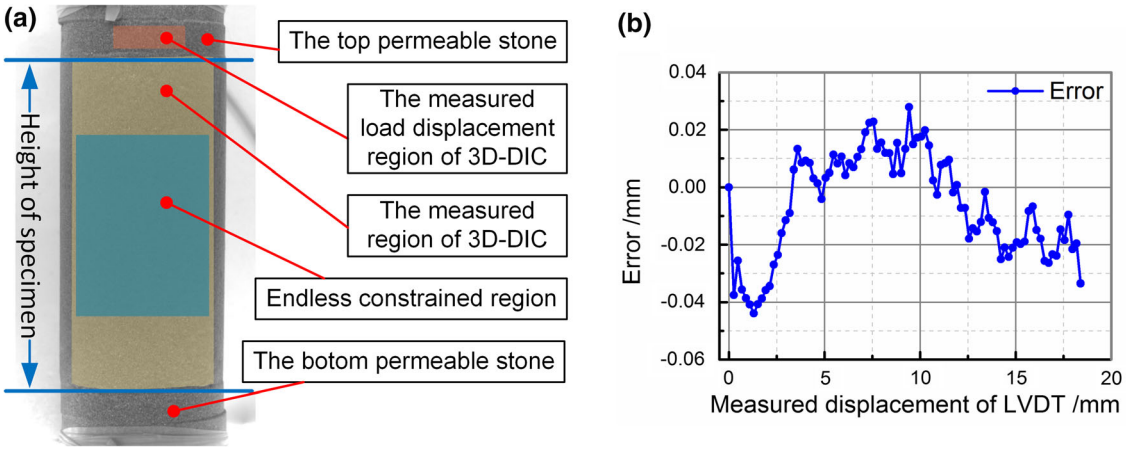

Fig. 4 **a** Different analysis region. **b** Vertical displacement error between 3D-DIC and LVDT in the HnCD-111 test (color figure online)

3 Measurement results

3.1 Measurement accuracy

Following the calibration of the stereovision system and distortion transformation from pixels to millimeters, the 3D data from the 3D-DIC can be applied to measure the deformation of the specimens in the tests. The specimens were compressed by the loading rod on top of the pressure chamber. Figure 4 shows several regions relevant to the measurement: the red region is on the top permeable stone for measuring the load displacement using 3D-DIC and has the same displacement with the loading rod as that measured by LVDT. The differences in the vertical axial displacement between the 3D-DIC and LVDT measurements (vertical error) are shown in Fig. 4b. The error is that the displacement obtained by 3D-DIC subtracts the displacement obtained by LVDT. It is observed that the error is

smaller than 0.04 mm. In the 3D-DIC measurement system, one pixel represents about 0.19 mm on the specimen, as shown in Table 2. The maximum value of the error is just about one-fifth of the length measured by one pixel. The yellow region is the measured region of 3D-DIC for measuring the deformation of the specimen, and the blue region is the middle of the specimen that is not affected by the end constraints. According to the research about end restraint of triaxial specimen by Liu et al. [15], the middle 45% region of the specimens is selected as the endless constrained region. Therefore, the relationship between stress and strain was obtained using the deformation of this region based on the 3D-DIC technique in the next section.

3.2 3D deformation of the specimens

Using the 3D-DIC technique, the displacement deformation field and the shape of the specimen all can be directly obtained during triaxial experiments. Of course, it is easy to obtain the local deformation intuitively. Figure 5a–e presents the specimen shape and vertical displacement deformation (unit: mm) corresponding to five moments (five red points) in the stress–strain curve of the HnCU-121, as shown in Fig. 5f, which is viewed from an Euler perspective. The global axial strain in Fig. 5f is the average axial strain of the endless constrained region. The positive value of the vertical displacement represents that the specimen is compressed in the geotechnical test. In these tests, the specimens were compressed by the loading rod with a constant strain rate of 0.2%/min. In the initial test, the vertical displacement occurs uniformly from the top of the specimen to the bottom and the shape of the specimen is almost a cylinder, as shown in Fig. 5a. With the loading increasing, the vertical displacement field becomes inhomogeneous gradually and the deformation of the specimen's shape increases gradually. Especially in Fig. 5e, the vertical displacement of the top specimen is larger than that in other specimen parts and a fracture line also can be

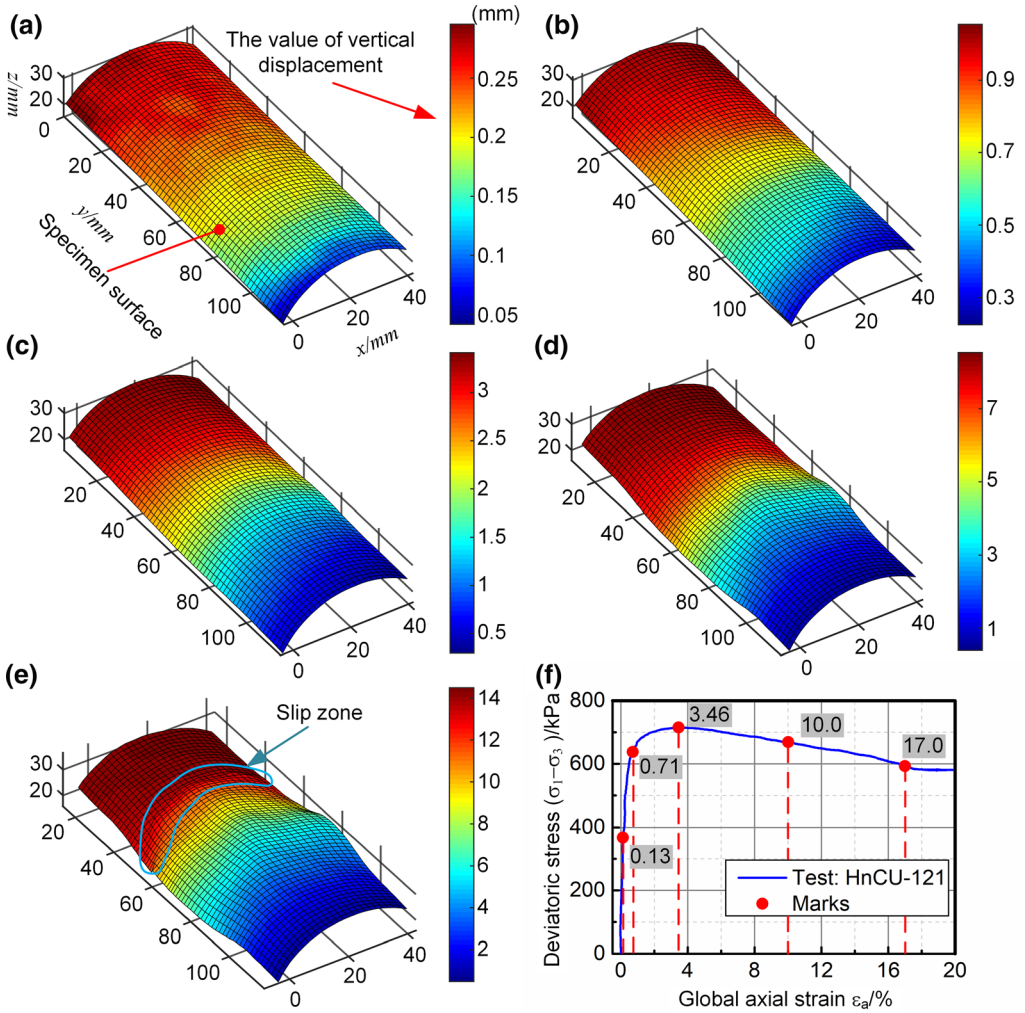

Fig. 5 **a**–**e** The vertical displacement and the specimen's contour that correspond to the five moments in **f**. **f** The global stress–strain curve of HnCU-121 measured by 3D-DIC (color figure online)

obviously observed on the specimen. Due to the end restraint, the shape variable at both ends of the specimen is not obvious, but there is obviously bulge in the middle of the specimen. Figure 5 presents the advantages of image measurement method which can obtain the local deformation of the measurement region.

Although the 3D displacement deformation of the specimen can be directly measured by the 3D-DIC, it is not enough to analyze the deformation characteristics of the triaxial specimen, because the strain is an important information in the material mechanics characteristic analysis. Usually, the axial strain can be calculated from the vertical displacement field through 3D-DIC, but specimen's radial strain can't be calculated directly. Because the entire cylindrical specimen cannot be completely covered by only a pair of cameras in the stereovision system, the cameras only cover approximately one-third of the cylindrical surface in this work. Moreover, the soil specimen is not a perfect cylinder. The calculation of the radial strain lacks a diameter reference. To solve this problem in triaxial test, an edge detection algorithm has been combined to the 3D-DIC algorithm to detect the specimen outline for obtaining the diameter or the axes of the specimen during the test. Due to the irregular and changing of the edge with the shape of the specimen, the edge detection algorithm must satisfy the accuracy and robustness. In addition, the speckle pattern on the specimen would also interfere with the recognition of the edge detection algorithm. The edge detection algorithm is easy to identify the black and white points of the speckle pattern as the edge. In this work, the edge detection based on structured forests has been adopted as the edge detection algorithm from trying many approaches. The edge detection is shown in Fig. 6a. The core of the method is based on the training of random decision forests. According to different occasions, the reliable edge detection would be obtained through training model parameters. The detailed principle of the edge detection algorithm has been described by Dollár et al. [7]. This method only reliably obtains the edge's grayscale based on the images and can't provide the accurate edge data for measurement. Therefore, the B-spline fitting has been applied to reaching to the subpixel accuracy, which would

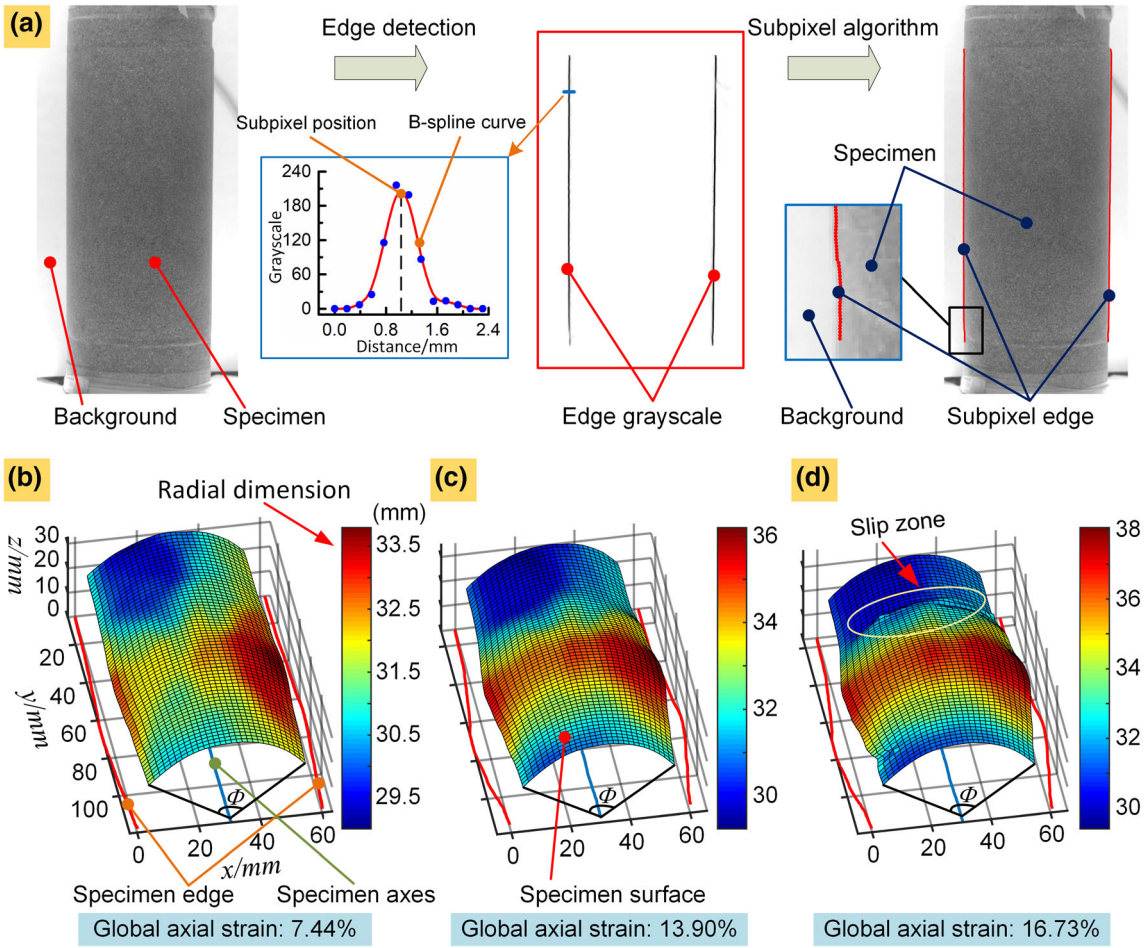

Fig. 6 **a** Realization of subpixel edge detection. **b–d** Radial dimension field of the specimen obtained by the 3D-DIC and the subpixel edge outline during the experiments at three global axial strains of 7.44%, 13.90%, and 16.73% in the HnCU-111 test (color figure online)

fit the smooth curve based on the grayscale of the discrete pixel [27]. The B-spline curve can be expressed as:

$$P(x) = \sum_{i=0}^{n} P_i F_{i,k}(x) \tag{2}$$

$$F_{i,k}(x) = \frac{1}{k!} \sum_{m=0}^{k-i} (-1)^m \binom{m}{k+1} (x + k - i - m)^k \tag{3}$$

Here, $P(x)$ is fitting curve equation; P_i is the coefficient value at ith discrete data points; k is the B-spline kernel order; m is the sequence number of the data points; $F_{i,k}(x)$ is the B-spline kernel value at $x - i$.

Figure 6a shows the process of the accurate specimen edge extracted by the subpixel edge algorithm in the HnCU-111 test. The grayscale of the edge has been detected by the edge detection algorithm based on the structured forests. Through the B-spline fitting, the curve of the discrete grayscale in horizontal direction has been fitted. The position of the peak of the curve is the position of the subpixel edge. When the boundaries are detected by the subpixel edge detection algorithm, the specimen axis is the center line of the two boundaries. Combining the specimens' surface, the volume of approximately one-third of the specimen can be calculated during the test. The radial dimension fields and the subpixel edge outlines of the specimen have been shown in Fig. 6b–d, which are obtained by the 3D-DIC and the subpixel edge detection algorithm at three global axial strains of 7.44%, 13.90%, and 16.73% in the HnCU-111 test. The initial average diameter of the specimen can be obtained using the edge detection algorithm. Therefore, the initial density and initial relative density can be calculated based on the initial mass values, as listed in Table 2.

Based on axis of the specimen obtained by the edge detection algorithm and displacement deformation field obtained by the 3D-DIC, the radial and axial strain distributions also can be calculated, as shown in Fig. 7. Figure 7 presents the radial and axial strain distributions of the four moments in the HnCU-121 test which corresponding to Fig. 5. Following the convention used in geotechnical engineering, the value of the radius reduction is positive and the value of radius extension is negative in the radial direction, while the axial compression is positive and axial extension is negative in the axial direction. The global axial strain shown in Fig. 5 represents the average axial strain in the blue region in Fig. 4a which is the middle 45% region of the specimen. In the initial test, the strain distribution is uniform in the radial and axial directions. With the loading, the specimen is compressed, and its compression is accompanied by radial expansion. The deformation is gradually inhomogeneous in the radial and axial directions. The large deformation is mainly concentrated in the middle region of the specimen. As shown in Fig. 5d, at the global axial strain of 17.0%, the maximum amplitudes of the axial strain and the radial strain reach 37.71% and 21.25%, respectively. The failure process shows obvious structure damage. Meanwhile, due to the boundary constraints, the deformation at both ends of the specimen is smaller than that in the middle of the specimen in the radial and axial directions. In particular, in Fig. 5d, a clear dividing line is observed in the specimen, which is considered to be the slip line or fracture line. In conventional experiments, the deformation of the whole specimen in the axial direction is measured by LVDT, while the radial deformation cannot be measured. Therefore, the influence of the boundary constraint in the strain measurements cannot be avoided. In the digital image measurement, the middle part of the specimen can be selected to analyze the mechanical properties of the soil, eliminating the end constraints.

4 Discussion

4.1 Inhomogeneous deformation of the specimen

According to the strain distributions, the probability density distributions of the axial strain obtained at several moments during the HnCD-131 test are presented in Fig. 8. In the initial experiment, the deformation is very small and there is the relative concentration of the strain probability. The phenomenon shows that the deformation is relatively uniform at global axial strain of 0.58%. This stage is in the pre-failure state. With continuous loading, the strain range gradually expands, as shown in Fig. 8b–d. The maximum strain value is several times larger than the minimum strain value. This process indicates that there is uneven deformation in the specimen and these phenomena usually occur near the peak stress. This stage can be treated as the in-failure state. In Fig. 8e–h, the density distribution of the strain probability is obviously divided into two parts. This press indicates that the specimen has been completely destroyed and the fracture or slip zone has been formed in the specimen. In the entire experiment, the deformation specimen shows structural behavior. Therefore, the global strain–stress curves from the conventional method cannot accurately quantify the inhomogeneous soil properties.

In the conventional triaxial test, the stress would be calculated by the loading and the area of the specimen's cross section. Due to the inability to measure the area, the area just can be calculated by the empirical equation and the end constraint also can't be eliminated. From Fig. 7, the deformation of the end of the specimen is limited obviously by the end constraints. Based on the image measurement technique, the middle 45% region has been

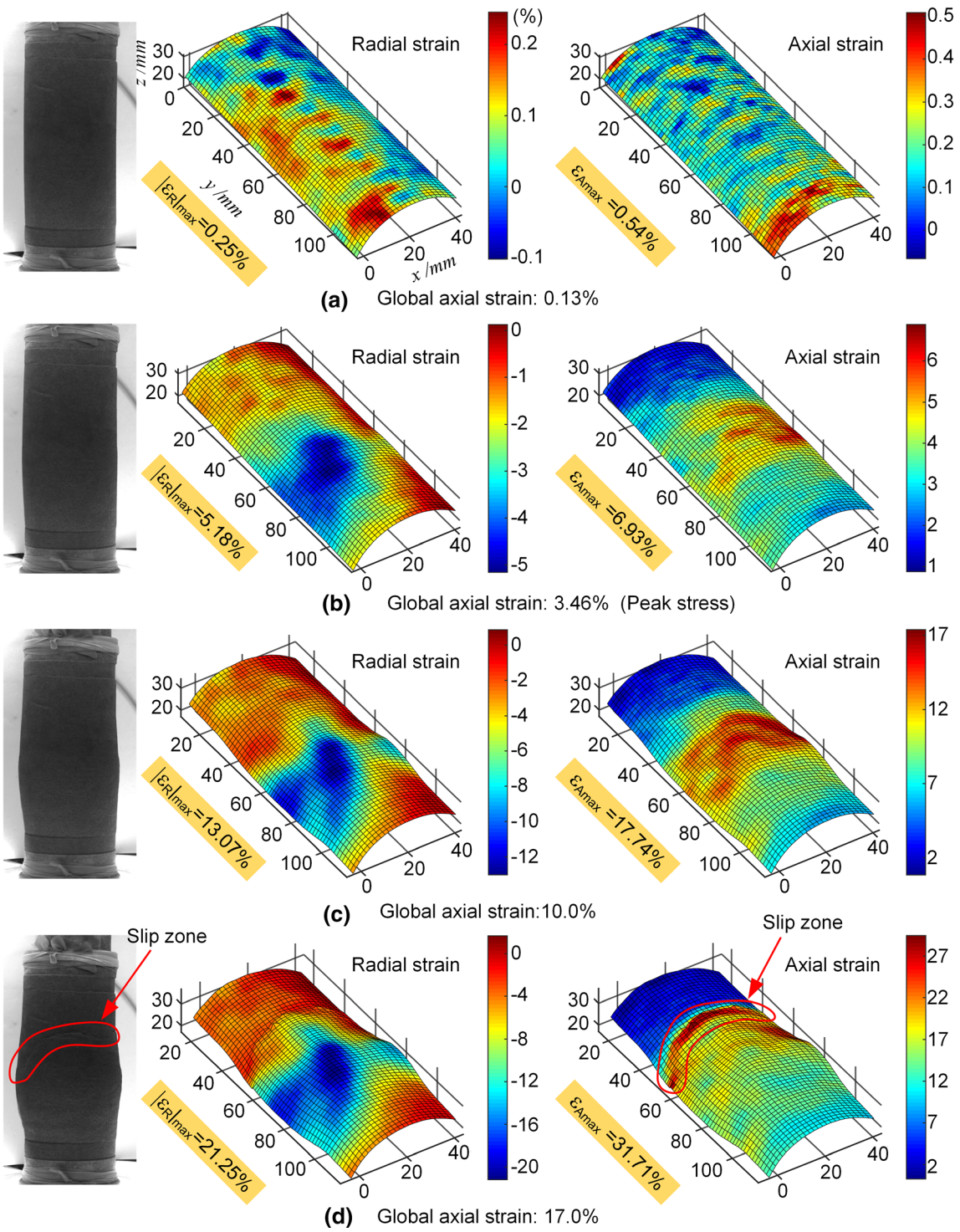

Fig. 7 **a–d** Radial and axial strain distributions measured by 3D-DIC during the HnCU-121 test (color figure online)

treated as the endless constrained region in this work. The deformation of the middle of the specimen can be measured directly and applied to calculating the specimen's stress. In order to validate the reasonableness of the endless constrained region, the average radial strain of the end and the middle of the specimen has been presented in Fig. 9. Five cross sections have been selected at 10%, 35%, 50%, 65%, 90% height of the specimen, respectively, as shown in Fig. 9a. The three cross sections in the middle are in the middle 45% region of the specimen which belongs to the endless constrained region. The other cross sections are at the top and bottom of the specimen, respectively.

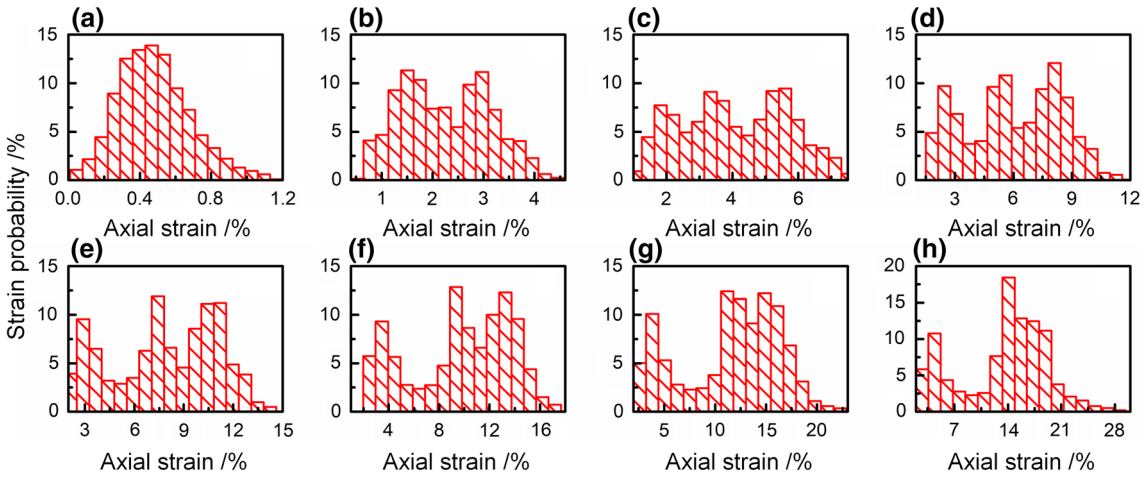

Fig. 8 **a–h** Strain probability density distributions at the global axial strains of 0.58%, 2.97%, 5.50%, 7.99%, 10.39%, 12.60%, 14.61% and 16.54% in the HnCD-131 test (color figure online)

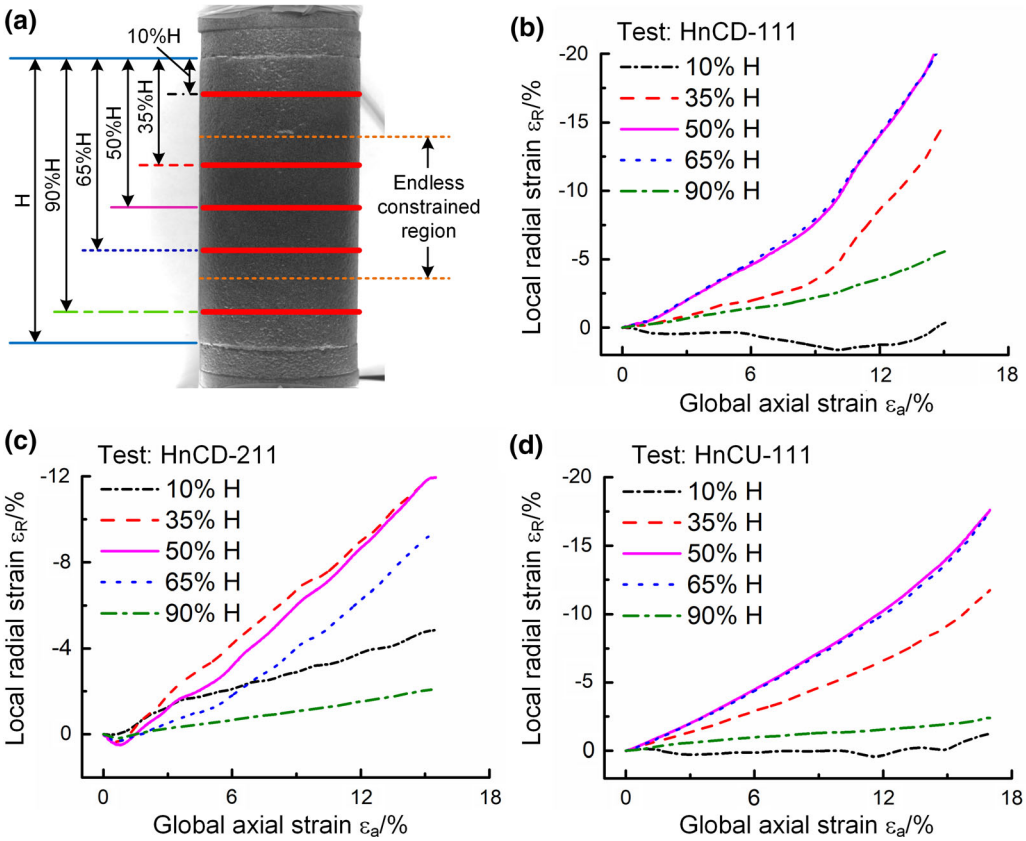

Fig. 9 **a** Five cross sections in the specimen. **b–d** The average radial strain curves of the five cross sections in the specimen obtained in the HnCD-111, HnCD-211, HnCU-111 test, respectively (color figure online)

Figure 9b–d presents the average radial strain at the different cross sections in the HnCD-111, HnCD-211, HnCU-111 test, respectively. In the HnCD-111 and HnCU-111 test, the specimens are in the dense state and the specimens' volume would expand during the test. From Fig. 9b, d, the radial strains at the end of the specimens are much smaller than that in the middle of the specimens. This indicates that the specimens' extension mainly occurs in the middle of the specimen in the dense state. For the specimens in the middle dense state, as shown in Fig. 8c, the specimens are softer than that in the dense state. The area of all the cross sections would expand during the test;

however, the radial strains in the middle of the specimens are still larger than that at the end of the specimen. Figure 9 indicates the deformation in the middle region of the specimen is similar, which can be treated as the endless constrained region.

4.2 Stress–strain behavior

To study the mechanical properties of geotechnical materials, it is necessary to obtain a stress–strain curve of the materials. In the conventional method, the values of stress and strain are usually computed according to the empirical equation. The force data and displacement data are obtained using load cells and LVDTs, respectively. Because the cross-sectional area change of the specimen cannot be directly obtained, the homogeneity assumption is used in the conventional method. Therefore, the error from the end constraints of the specimen cannot be avoided. By contrast, using the image measurement method, the specimen deformation can be directly measured. The radial dimension can be measured with continuous loading, as shown in Fig. 8. To avoid the effects of the specimen end constraints, the middle 45% regions of the specimen are selected as the unconstrained region, as shown in blue in Fig. 4a. When the stress is calculated, the area is the average value of the middle 45% region of the specimens. Figure 10 presents the stress–strain curves of the tests in Table 2 by the conventional sensors and 3D-DIC. It is observed from Fig. 10 that the deformations measured by 3D-DIC are usually larger than those measured by the conventional method in the experiments and the all of the peak stresses measured by 3D-DIC are smaller than those measured by the conventional method. At the same time, the strain corresponding to the peak position is smaller. The specimen in HnCD-211 test in the middle dense state, its stress has been increasing during the test, as shown in Fig. 10a, but its stress measured by the conventional method is still larger than that measured by 3D-DIC. Because the radial strain can't be measured, the deformation is treated as the uniform during the test in the conventional method. In the image measured method, the middle region of the specimen is selected, whose deformation wouldn't be affected by the end constraints. At the same time, the area of the middle region can be measured directly. The results obtained by image measurement method are more reliable than that obtained by the conventional method. From Fig. 10, the sand specimens would actually be destroyed earlier and the strength of the specimen is overestimated in the conventional method. According to the stress–strain curves in consolidated undrained tests in Fig. 10b, due to the negative pressure occurred in the undrained tests, the strength of the sand specimens is raised, especially in the post-failure stage.

4.3 Local volume strain

Combining the edge detection algorithm and 3D-DIC, this method will obtain the local volume and the volume strain. The volume overlapped by the stereovision system can be calculated by integration in the cylindrical coordinates system at each point in time, as expressed by Eq. (4).

$$V = \int_0^H \int_0^\Phi \int_0^R r \cdot \mathrm{d}r \cdot \mathrm{d}\varphi \cdot \mathrm{d}h \tag{4}$$

Here, H is the current height of specimen, Φ is the angle of measured curved surface, as shown in Fig. 6b–d, and R is the radius of the specimen cross section.

In the conventional method, the volume changes of a saturated soil specimen in undrained test are measured using a burette in the drained condition. Because the only one stereovision system has been used in the work, the volume strain of the cameras covered region represents the global volume strain of the specimen. To validate the

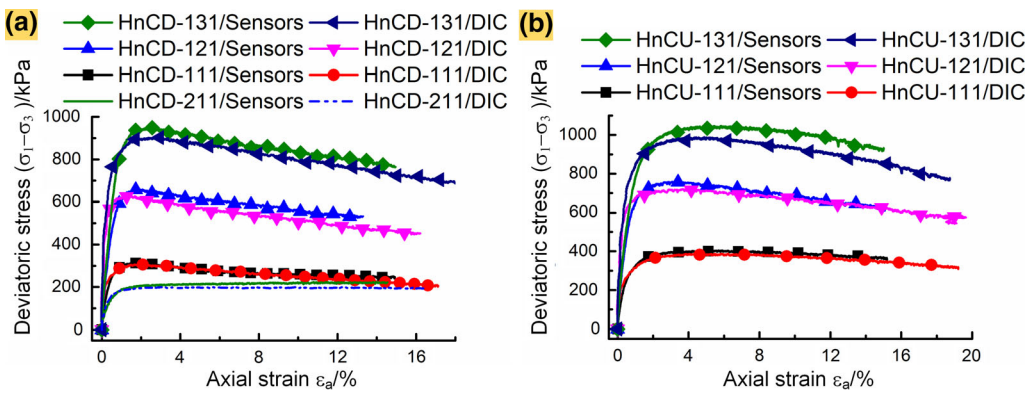

Fig. 10 **a** Stress–strain curves measured by conventional sensors and 3D-DIC in the drained conditions. **b** Stress–strain curves measured by conventional sensors and 3D-DIC in the undrained conditions (color figure online)

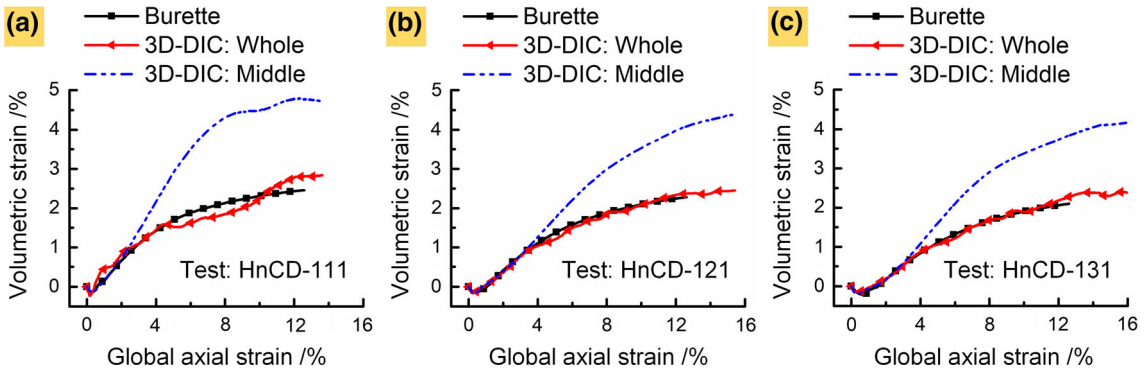

Fig. 11 **a–c** Volumetric strain measured by the conventional method and 3D-DIC under the drained condition (color figure online)

accuracy of the results measured by the image measurement method, the results are compared with the results of the burette in the draining experiments for HnCD-111, HnCD-121 and HnCD-131, as shown in Fig. 11. Figure 11 presents three kinds of volume strain: the global volume strain measured by the conventional method and the proposed method, the volume strain of the middle of the specimen measured by the proposed method. The negative volumetric strain represents specimen extension and the positive volumetric strain represents specimen contraction. In the experiments, the volume of the entire specimen during the loading process first decreased and then increased. The curves are consistent with the sand specimens in dense state, and the global volume strain measured by the two kinds of measurement methods is very similar. Comparison to the results obtained by the burette also proved that the results obtained by the proposed method are reasonable. However, the curves of the image and burette measurements are different in the later stage of the experiments. The reasons are that the measuring region of 3D-DIC just cover approximately one-third of the cylindrical surface of the specimen in this work and the nonuniform deformation of the specimen is becoming more and more serious during the test. The volume deformation in the middle of the specimen is similar to the global volume deformation in the earlier stage of the tests. However, due to the middle endless constrained region, the middle volume strain is growing faster than the entire volume strain with the loading. Therefore, due the end constraints, the volume measured by the burette in the triaxial test can't reflect the real volume deformation of the specimen. The image measurement method can obtain the deformation of the middle of the specimen which is the endless constrained region, and the results are more reasonable than that measured by the conventional method. However, the results measured by the conventional method are still reasonable in the earlier stage of the test.

5 Conclusion

In this paper, a digital image measurement system is constructed based on a triaxial apparatus investigated and developed in our laboratory. Even though only a pair of cameras is applied to measure the cylindrical specimen, the full-field deformation and volumetric strains of the specimen can be accurately obtained in triaxial testing using the 3D-DIC technique and a subpixel edge detection algorithm. Through the stereovision calibration procedure, not only the inhomogeneous deformation is directly observed in triaxial testing, but also the local strain distribution and local volume strain of the specimen can be accurately quantified. Compared to the conventional method in triaxial test, the experimental results measured by the proposed method provide more detailed deformation information. Based on Hainan (China) sand samples, the proposed method can obtain the stress–strain relationship and the volume strain in the endless constrained region. Due to the accuracy and inexpensiveness of the image measurement method, we are trying to apply this method to developing a soil's constitutive model and other geotechnical tests, for example, the unsaturated soil triaxial test and dynamic triaxial tests.

Acknowledgements This work was supported by the National Natural Science Foundation of China (Nos. 51309047 and 51975082).

References

1. Alikarami R, Andò E, Gkiousas-Kapnisis M, Torabi A, Viggiani G (2014) Strain localisation and grain breakage in sand under shearing at high mean stress: insights from in situ X-ray tomography. Acta Geotech 10(1):15–30. https://doi.org/10.1007/s11440-014-0364-6
2. Blatz J, Graham J (2003) Elastic–plastic modelling of unsaturated soil using results from a new triaxial test with controlled suction. Géotechnique 53(1):113–122. https://doi.org/10.1680/geot.2003.53.1.113
3. Chen R, Ng CWW (2013) Impact of wetting–drying cycles on hydro-mechanical behavior of an unsaturated compacted clay. Appl Clay Sci 86:38–46. https://doi.org/10.1016/j.clay.2013.09.018

4. Chen F, Chen X, Xie X, Feng X, Yang L (2013) Full-field 3D measurement using multi-camera digital image correlation system. Opt Lasers Eng 51(9):1044–1052. https://doi.org/10.1016/j.optlaseng.2013.03.001
5. Chen W-B, Yin J-H, Feng W-Q (2018) A new double-cell system for measuring volume change of a soil specimen under monotonic or cyclic loading. Acta Geotech. https://doi.org/10.1007/s11440-018-0629-6
6. Cheng Z, Wang J (2019) Quantification of the strain field of sands based on X-ray micro-tomography: a comparison between a grid-based method and a mesh-based method. Powder Technol 344:314–334. https://doi.org/10.1016/j.powtec.2018.12.048
7. Dollár P, Zitnick CL (2015) Fast edge detection using structured forests. IEEE Trans Pattern Anal Mach Intell 37(8):1558–1570. https://doi.org/10.1109/TPAMI.2014.2377715
8. Harris CG, Stephens M (1988) A combined corner and edge detector. In: Alvey vision conference, vol 50. Citeseer, pp 10–5244
9. Hartmann C, Wang J, Opristescu D, Volk W (2018) Implementation and evaluation of optical flow methods for two-dimensional deformation measurement in comparison to digital image correlation. Opt Lasers Eng 107:127–141. https://doi.org/10.1016/j.optlaseng.2018.03.021
10. Hasan A, Alshibli KA (2010) Experimental assessment of 3D particle-to-particle interaction within sheared sand using synchrotron microtomography. Géotechnique 60(5):369–379. https://doi.org/10.1680/geot.2010.60.5.369
11. Higo Y, Oka F, Sato T, Matsushima Y, Kimoto S (2013) Investigation of localized deformation in partially saturated sand under triaxial compression using microfocus X-ray CT with digital image correlation. Soils Found 53(2):181–198. https://doi.org/10.1016/j.sandf.2013.02.001
12. Kido R, Higo Y (2017) Evaluation of distribution of void ratio and degree of saturation in partially saturated triaxial sand specimen using micro X-ray tomography. Jpn Geotech Soc Spec Publ 5(2):22–27. https://doi.org/10.3208/jgssp.v05.006
13. Laloui L, Peron H, Geiser F, Rifa A, Vulliet L (2006) Advances in volume measurement in unsaturated soil triaxial tests. Soils Found 46(3):341–349. https://doi.org/10.3208/sandf.46.341
14. Li L, Zhang X (2019) Factors influencing the accuracy of the photogrammetry-based deformation measurement method. Acta Geotech 14(2):559–574. https://doi.org/10.1007/s11440-018-0663-4
15. Liu X, Shao L, Guo X (2013) Local data analysis for eliminating end restraint of triaxial specimen. Trans Tianjin Univ 19(5):372–380. https://doi.org/10.1007/s12209-013-2000-1
16. Messerklinger S, Springman SM (2007) Local radial displacement measurements of soil specimens in a triaxial test apparatus using laser transducers. Geotech Test J 30(6):454–465
17. Mousa A (2017) Revisiting the calibration philosophy of constitutive models in geomechanics. Int J Geomech 17(8):06017002
18. Nawir H, Apoji D, Ekawita R, Khairurrijal K (2018) Axial and lateral small strain measurement of soils in compression test using local deformation transducer. J Eng Technol Sci 50(1):53–72. https://doi.org/10.5614/j.eng.technol.sci.2018.50.1.4
19. Ng CWW, Zhan LT, Cui YJ (2002) A new simple system for measuring volume changes in unsaturated soils. Can Geotech J 39(3):757–764. https://doi.org/10.1139/t02-015
20. Pan B, Li K, Tong W (2013) Fast, robust and accurate digital image correlation calculation without redundant computations. Exp Mech 53(7):1277–1289. https://doi.org/10.1007/s11340-013-9717-6
21. Rechenmacher AL, Abedi S, Chupin O, Orlando AD (2011) Characterization of mesoscale instabilities in localized granular shear using digital image correlation. Acta Geotech 6(4):205–217. https://doi.org/10.1007/s11440-011-0147-2
22. Salazar S, Miramontes L, Barnes A, Bernhardt-Barry M, Coffman R (2019) Verification of an internal close-range photogrammetry approach for volume determination during triaxial testing. Geotech Test J . https://doi.org/10.1520/GTJ20170125
23. Shao LT, Liu G, Zeng FT, Guo XX (2016) Recognition of the stress–strain curve based on the local deformation measurement of soil specimens in the triaxial test. Geotech Test J 39(4):658–672. https://doi.org/10.1520/gtj20140273
24. Sutton MA, Wolters WJ, Peters WH, Ranson WF, McNeill SR (1983) Determination of displacements using an improved digital correlation method. Image Vis Comput 1(3):133–139. https://doi.org/10.1016/0262-8856(83)90064-1
25. Sutton MA, Orteu JJ, Schreier H (2009) Image correlation for shape, motion and deformation measurements: basic concepts, theory and applications. Springer, Berlin. https://doi.org/10.1007/978-0-387-78747-3
26. Tang Y, Okubo S, Xu J, Peng S (2019) Progressive failure behaviors and crack evolution of rocks under triaxial compression by 3D digital image correlation. Eng Geol 249:172–185. https://doi.org/10.1016/j.enggeo.2018.12.026
27. Unser M, Aldroubi A, Eden M (1993) B-spline signal processing. I. Theory. IEEE Trans Signal Process 41(2):821–833. https://doi.org/10.1109/78.193220
28. Wang H, Sato T, Koseki J, Chiaro G, Tan Tian J (2016) A system to measure volume change of unsaturated soils in undrained cyclic triaxial tests. Geotech Test J 39(4):532–542. https://doi.org/10.1520/GTJ20150125
29. Wang P, Sang Y, Shao L, Guo X (2019) Measurement of the deformation of sand in a plane strain compression experiment using incremental digital image correlation. Acta Geotech 14(2):547–557. https://doi.org/10.1007/s11440-018-0676-z
30. Witowski M (2018) Local displacement transducer with miniature position encoder. Geotech Test J 41(6):1147–1154. https://doi.org/10.1520/GTJ20170016
31. Xiao H, Lee FH, Yao K, Ho J, Liu Y (2019) Miniature LVDT setup for local strain measurement on cement-treated clay specimens. Mar Georesour Geotechnol 37(8):989–998. https://doi.org/10.1080/1064119X.2018.1460428
32. Yuan Y, Zhan Q, Xiong C, Huang J (2017) Digital image correlation based on a fast convolution strategy. Opt Lasers Eng 97:52–61. https://doi.org/10.1016/j.optlaseng.2017.05.010
33. Zeng F, Shao L (2016) Unloading elastic behavior of sand in cyclic triaxial tests. Geotech Test J 39(3):20150171. https://doi.org/10.1520/gtj20150171
34. Zhang Z (2000) A flexible new technique for camera calibration. IEEE Trans Pattern Anal Mach Intell 22(11):1330–1334. https://doi.org/10.1109/34.888718
35. Zhang X, Mavroulidou M, Gunn MJ, Sutton J, Cabarkapa Z, Kichou Z (2013) Application of a novel laser sensor volume measurement system to the triaxial testing of an unsaturated lime-treated soil. Acta Geotech 9(6):945–957. https://doi.org/10.1007/s11440-013-0254-3
36. Zhang X, Li L, Chen G, Lytton R (2014) A photogrammetry-based method to measure total and local volume changes of unsaturated soils during triaxial testing. Acta Geotech 10(1):55–82. https://doi.org/10.1007/s11440-014-0346-8
37. Zielinski M, Sánchez M, Romero E, Atique A (2014) Precise observation of soil surface curling. Geoderma 226–227:85–93. https://doi.org/10.1016/j.geoderma.2014.02.005

Publisher's Note Springer Nature remains neutral with regard to jurisdictional claims in published maps and institutional affiliations.